Influence of initial crystalline phase of TiO2 to obtain TiN thin films from sol-gel route by rapid thermal nitridation process

Victor Vallejo-Otero, Arnaud Valour, Hugo Bruhier, Yannick Bleu, Nadège Ollier, Emilie Gamet, Yaya Lefkir, Christophe Donnet, Nicolas Crespo-Monteiro, Yves Jourlin

Influence of Initial Crystalline Phase of TiO_2 to Obtain TiN Thin Films from Sol-Gel Route by Rapid Thermal Nitridation Process.

Victor Vallejo-Otero, Arnaud Valour, Hugo Bruhier, Yannick Bleu, Nadège Ollier, Yaya Lefkir, Christophe Donnet, Nicolas Crespo-Monteiro, Yves Jourlin**

Université Jean Monnet Saint-Etienne, CNRS, Institut d'Optique Graduate School, Laboratoire Hubert Curien UMR5516, F-42023, SAINT-ETIENNE, France.

E-mail : nicolas.crespo.monteiro@univ-st-etienne.fr; yves.jourlin@univ-st-etienne.fr

Keywords: Titanium nitride, sol-gel method, Rapid Thermal Nitridation

ABSTRACT

Titanium Nitride (TiN) is widely used in many industrial sectors for its outstanding performances including its mechanical properties, high chemical and thermal stability. Associated with its plasmonic behavior, TiN thin films are very promising for the manufacturing of optical metasurfaces devices or new plasmonic materials. Among the processes that make it easy to obtain metal nitride coatings, nitriding of metal oxide films has become increasingly popular in recent years. A multitude of synthesis processes can be used to obtain TiO_2 films, with different crystalline states (amorphous, anatase or rutile) depending on the technique used, which can then be converted into TiN coatings. In this paper, the effect of the initial crystalline state of TiO_2 layers was investigated on the structural properties, plasmonic properties and the friction behavior of TiN thin films obtained by Rapid Thermal Nitridation (RTN). The results indicate that, regardless of the crystalline state of the starting TiO_2 film, the RTN process leads to complete nitridation of TiN coating. Moreover, even though surface morphology and friction properties differ slightly, depending on the crystallization of the starting TiO_2, plasmonic properties remain very similar, thus highlighting the great versatility and uniformity of this nitriding technique, enabling TiN to be produced for a wide range of applications.

1. INTRODUCTION

In recent years, demand has been growing for materials with very high thermal, mechanical, optical and electrical properties, and this has led to a significant focus on advanced ceramics. Such high performances can be achieved by non-oxide composite including carbide and/or nitride [1–3]. Among these new materials, titanium nitride (TiN) has received the most attention particularly due to its mechanical [4] and plasmonic properties [5–7]. Such coatings can be micro and nano structured, thereby conferring new functionalities and properties, for example, optical[8,9] and mechanical[10] properties leading to new metamaterials and metasurfaces [11–13].

Various methods can be used to obtain TiN thin films that involve vacuum technology and either physical vapor deposition (PVD) or chemical vapor deposition (CVD). These methods include reactive magnetron sputtering [14–17] , molecular-beam epitaxy [18,19], chemical vapor deposition [20,21], atomic layer deposition [22–24], and pulsed laser deposition [25–27]. The source of the titanium needed for these deposition techniques can be Ti, TiN or $TiCl_4$ for example [28–30]. These methods are ideally suited to produce homogeneous coatings without structuring. However, due to their intrinsic properties, and notably their mechanical and chemical ones, surface micro-nanostructuring of metal nitrides is usually difficult. Some tools are available for structuring them, such as those used in microelectronics (lithography, etching, lift-off), but these technologies are costly and/or time and energy-consuming and are not always suitable for large surfaces and/or unconventional shapes, thus limiting technological developments and economic and industrial spin-offs.

Another type of technique used to produce TiN is reduction and nitridation of TiO_2. This technique comprises the reaction of reduction of the TiO_2 followed by a reaction between a nitrogen source and the reduced product at high temperatures. Typically, the nitridation of TiO_2 films is accomplished using conventional ovens, but requires prolonged exposure to high temperatures (exceeding 900-1000 °C for several hours) [31,32] and an extra reductant [33,34]. The advantage of this method is that TiO_2 is much easier to structure than TiN, thus enabling the production of more complex structures. Its disadvantages are the need to use high-temperature-resistant substrates and the relatively long processing time (several hours), which limits its industrial application. We recently developed a rapid thermal nitridation technique (RTN) to nitridate TiO_2 thin films with ammonia gas using a rapid thermal annealing (RTA) oven [6,7,35]. During this process TiO_2 sol-gel layers are irradiated by infrared flashes with a flow of NH_3. The flashes are absorbed by the sample, thereby heating it, and, due to the presence of NH_3 nitridation occurs. The use of an RTA oven makes it possible to reduce the nitridation process from several hours using a conventional furnace, to 10 to 15 minutes. The advantages of this technique are a very short processing time (compatible with industrial development), a process that can potentially limit thermal damage to the substrates (flash infrared), and the use of the sol-gel route to produce the TiO_2 samples.

The sol-gel route is widely used in materials chemistry to produce a broad range of inorganic materials [36,37] in different forms including powders [38], fibers [39], dense films [40] and xerogels [6]. Depending on the process, the crystalline phase of TiO_2 can vary between amorphous, anatase and rutile [39,41–43]. Some studies have shown that the initial states of the TiO_2 can have an impact on the TiN films produced after nitridation [44–46]. However, these studies were only performed using high temperature ovens, under treatments that lasted for several hours, and included the incorporation of a reductant (carbothermal reduction) to facilitate nitriding[44–46], all of which further restrict potential fields of application.

In this paper, we first focus on the possibility of nitridation of the crystalline phases (amorphous, anatase and rutile) of TiO_2. We analyze and compare the nitrided films with TiN films reported in the literature. Raman spectroscopy and X-ray diffraction will be employed to compare the crystal structure of each sample. Second, we assess the effect of the initial crystalline state of the TiO_2 on the plasmonic properties and the friction behavior of TiN thin films obtained by RTN. We use UV, visible, near-IR spectroscopy, as well as ellipsometry to study the optical properties. Finally, we use a linear reciprocating tribometer to measure the friction properties.

2. MATERIAL AND METHODS

2.1 Production of TiO_2 films

To produce the titania thin films, two sols were mixed using a specific sol-gel technique previously published and detailed in the references [6,35,36]. Briefly, the first sol was prepared by reacting Titanium (IV) Isopropoxide (TIPT purchased from Aldrich) with deionized water, hydrochloric acid (HCl from Roth), and butyl alcohol (BuOH from Alfa Aesar) as a solvent. The concentration of TIPT in the solution was 0.4 M, and the TIPT/H_2O/HCl/BuOH molar composition was 1/0.82/0.13/23.9. The second sol was prepared from TIPT complexed by benzoylacetone (BzAc from Aldrich) in ethyl alcohol (EtOH from Sigma-Aldrich). The TIPT/BzAc/EtOH molar composition was 1/0.91/20.4. TiO_2 sol-gel was obtained by mixing the two sols to form a final sol with a TIPT concentration of 0.6 M and a BzAc/TIPT molar ratio of 0.6. The TiO_2 sol was coated on a silicate substrate by spin-coating at 3000 rpm for 30 s.

The resulting sol-gel film was heat-treated in air at 110 °C, 400 °C and 800 °C for 90 min. The thickness of each sample was measured by profilometry using a Veeco Dektak 3 ST profilometer.

2.2 Rapid thermal nitridation of Titania thin films

A rapid thermal nitridation treatment was then applied to the different heat-treated TiO_2 layers in a reproducible and uniform process using pure NH_3 gas (purity 99.98% from Linde Gas). Nitridation occurs at high temperatures in a halogen infrared lamp-heated furnace (RTA As-One 100 from Annealsys). After a purge of the reactor with N_2 and vacuum sealing, the samples underwent 10 cycles, each cycle including 30 s of high irradiation (45% of the lamp power) and 5 s of low irradiation (1% of the lamp power). The alternating cycles of high and low irradiation protect the lamps from premature dysfunction. During the nitridation process, a NH_3 flow (1000 sccm) was introduced in the chamber at a pressure of 10 mbar. The nitridation parameters were chosen based on the results of previous studies of rapid thermal nitridation of TiO_2 [6,7,35]. The conditions were adjusted for the present study, but there is still scope for further optimization.

2.3 Optical measurements

Spectrophotometric measurements were taken before and after nitridation (Cary 5000 UV–Vis–NIR from Agilent Technologies). The measurements were performed in the wavelength range between 200 and 2000 nm, in reflectance with an angle of incidence of 10° and in transmittance with normal incidence.

The thickness, the refractive index (n) and the extinction coefficient (k) of the nitridated samples were measured by ellipsometry (SEMILAB Sopra GES-5E). The measurements were taken using an angle of incidence of 70° between 300 and 1000 nm. The optical model consists of two layers on a semi-infinite silica glass substrate. The first layer was made of the material under consideration (TiN with porosity). The second layer is considered as a roughness layer, with a 50%–50% mixed dielectric function between void and the dielectric function of the first layer, as schematized in Figure 1. The dispersive law used to model the complex dielectric function of the TiN film is a standard dispersion model based on the sum of a Drude and two Lorentz oscillators [47–49]. Effective medium models were used to modelized the porosity and the roughness of the TiN films: The Maxwell-Garnett

model was used to model the porosity of the TiN layer [50] and the Bruggeman model to model surface roughness [51].

For comparison, the thickness of the film in each nitridated sample was also measured with a Veeco Dektak 3 ST profilometer.

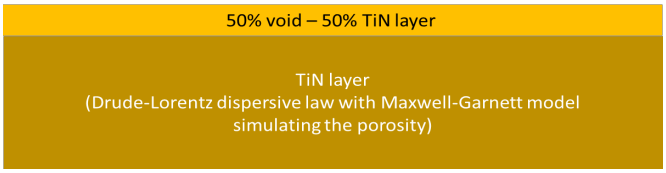

Figure 1: *Schematic diagram of the optical ellipsometry model of the TiN layers.*

2.4 Structural properties and surface morphology.

The phase composition and crystalline structure of the thin films before and after the nitridation process were analyzed using Raman micro spectroscopy measurements (LabRam ARAMIS) with excitation at 633 nm (He-Ne laser) and X-ray diffraction (GIXRD). The diffractograms were obtained using a PANalytical AERIS diffractometer. The X-ray beam used was produced by a copper anti-cathode, with a wavelength of 0.154 nm and a power of 450W (15mA, 30 kV). The grazing incidence angle of the X-ray beam was 0.4°. Acquisition was performed between 2θ=20° and 2θ=85°, with a step size of 0.04°.

The surface morphologies of the thin films were characterized by atomic force microscopy (AFM) measurements (Dimension Icon, Bruker company, Billerica, MA, USA) in tapping mode and by scanning electron microscopy (SEM) with a JSM-IT80 (from JEOL) with a UHD detector.

2.5 Friction measurements

To test the friction resistance of the TiN film, tribological measurements were taken with a linear reciprocating tribometer (Anton Paar TRB3) in ambient air at room temperature. The different TiN films deposited on a silica glass substrate were in sliding contact with a mirror polished AISI 52100 steel ball (diameter 6 mm) at a linear speed of 1 $mm.s^{-1}$ along a 2 mm wear track length. A normal force of 1 N was applied in the contact region, consistent with mean and maximum Hertzian contact pressures of 266 and 400 MPa, respectively, and a Hertzian contact diameter of 70 µm.

3. RESULTS AND DISCUSSION

3.1 Titania Films

Three TiO_2 films were prepared by spin coating of TiO_2 sol-gel at 3000 rpm for 30s on SiO_2 substrate. These films were then thermally treated differently. The first was heated at 110°C for 90min and the second and the third respectively at 400°C and 800°C for 90min in order to have 3 samples with different initial conditions for the nitridation process.

3.1.1 Optical properties

After deposition and thermal treatment, the three TiO_2 samples were transparent and homogeneous in transmittance, however transmittance decrease with increase in temperature (Figure 2A). The main difference observed on the transmittance spectrum of each sample is around wavelength 500 nm. Indeed, after a maximum of transmission at around 500 nm (90% for TiO_2 treated at 110°C and 400°C and 80% for TiO_2 treated at 800°C) there was a decrease in transmission. Minima of 85%, 75% and 60% were attained at 600 nm, 900 nm and 760 nm for the TiO_2 treated at respectively, 110°C, 400°C and 800°C. The absorption edges of anatase (400°C) and rutile (800°C) TiO_2 thin film were blue-shifted by respectively, about 65 and 35 nm, compared with that of the amorphous TiO_2 film. The associated direct band gap energies of samples treated at 110°C, 400°C and 800°C were estimated to be 3.1, 3.7 and 3.4 eV [52].

In reflectance, the films took on different colors (Figure 2B). Indeed, while the TiO_2 treated at 110°C took on a greenish color in reflection, the TiO_2 treated at 400°C and 800°C took on respectively a pinkish and a yellowish color. These colors are interferometric colors that vary depending on the thickness and index of the films. The thickness of the TiO_2 film annealed at 110°C was close to 300 nm (± 20 nm), and when annealed at 400°C and 800°C, the thickness was around 50 nm (± 10 nm). As expected from the color in reflection, the reflectance spectrum presented in Figure 2B revealed significant differences among the samples. The TiO_2 treated at 110°C presented low reflectance that did not exceed 20%. The TiO_2 treated at 400°C and 800°C are similarly curved in shape even though the latter had a maximum reflectance of 40% at 750 nm, whereas at the same wavelength, the former had a reflectance of 25%. Furthermore, both TiO_2 treated at 110°C and at 400°C showed a dip at 500 nm. The same dip was present on the spectrum of the TiO_2 treated at 800°C but with a shift to a lower wavelength (minimum at 470 nm).

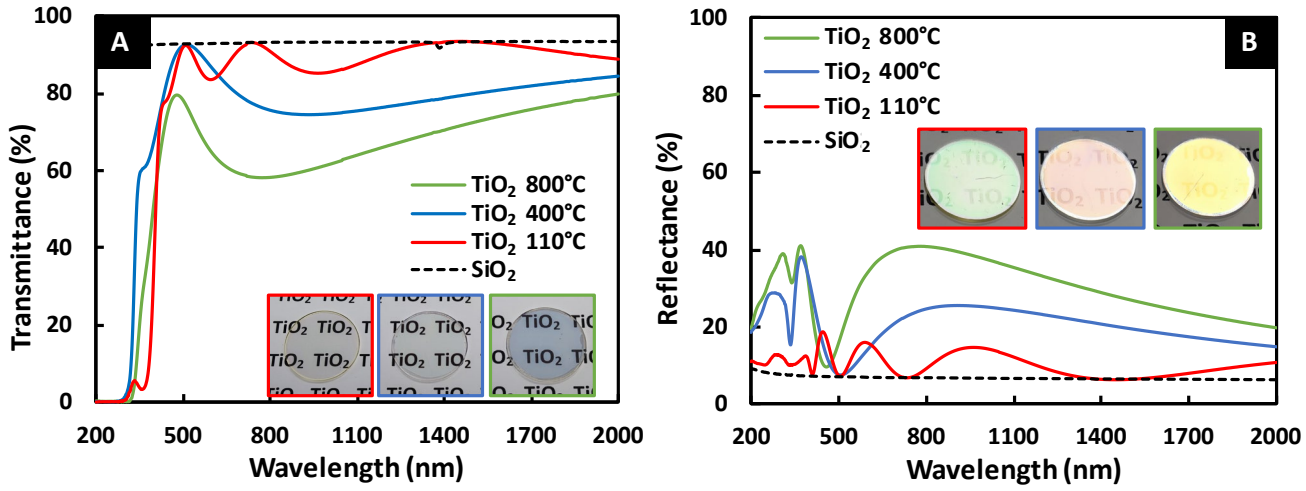

Figure 2: *(A) UV–Visible-NIR transmittance and (B) reflectance spectra of the SiO_2 substrate and TiO_2 layers thermally treated in air at 110°C, 400°C and 800°C during 90min. Inset: optical photographs of the different TiO_2 thin films in specular transmission and reflection, respectively.*

3.1.2 Structural properties and surface morphology

Grazing incidence X-ray diffraction (GIXRD) measurements were taken on the thermally treated TiO_2 films, and the diffractograms are shown in Figure 3A. The GIXRD pattern of titania film thermally treated in air at 110°C (in red) revealed the absence of diffraction peaks related to crystallized phases of titania, underlining the amorphous character of this titania film. These results are in agreement with the Raman analysis of the same sample shown (in red) in Figure 3B. Indeed, the spectrum exhibits various small active modes related to the BzAc or TiO_2/BzAc complex but no features of crystallized TiO_2, confirming its amorphous nature [35,53].

The GIXRD pattern of the TiO_2 layer annealed at 400 °C (in blue in Figure 3A) indicates the formation of structure-type anatase (JCPDS file 96-720-6076). The Raman spectrum corresponding (in blue in Figure 3B) presents the five Raman active modes (at 142, 195, 398, 515 and 640 cm^{-1}) related to the anatase phase [54,55], confirming the sole presence of this phase.

After heat treatment in air at 800 °C, the titania layer displayed diffraction peaks (in green in Figure 3A) well indexed to the Rutile structure (JCPDS file 96-600-1682). Its corresponding Raman spectrum (in green in Figure 3B) displayed the four main Rutile Raman vibration modes (at 148, 240, 445 and 610 cm^{-1}). The observed Raman peaks are consistent with reports in the literature [55,56]. To summarize, the film thermally treated in air at 110 °C is amorphous, the film treated at 400 °C is anatase, and the film treated at 800 °C is rutile. The associated direct band gap energies of samples treated at 110°C, 400°C and 800°C estimated above are in agreement with the values reported in the literature for amorphous, anatase and rutile phase [57].

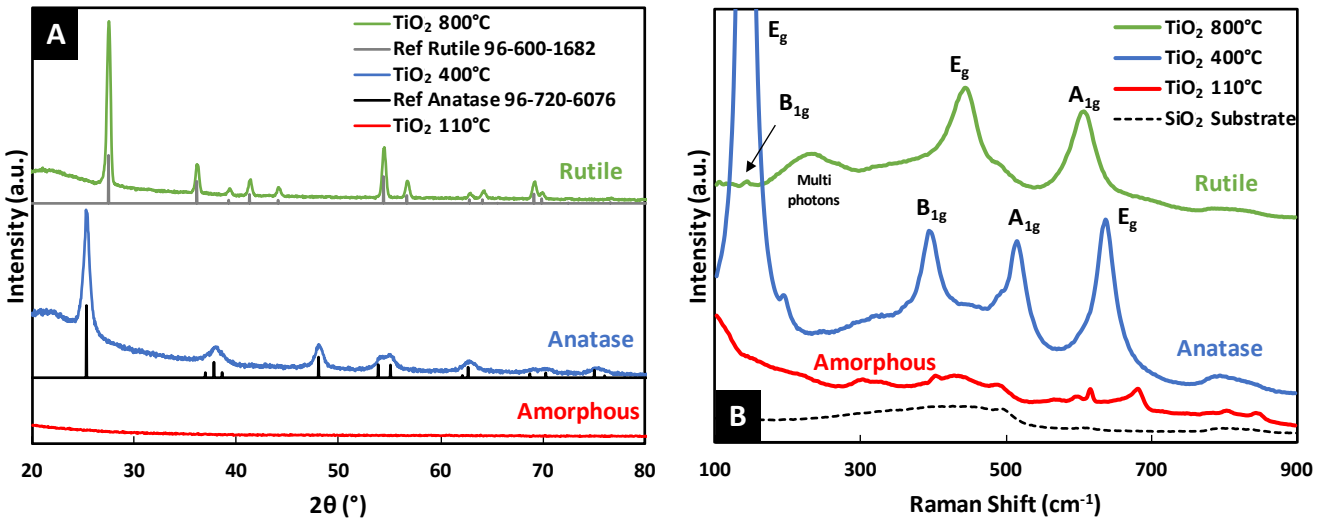

Figure 3: *(A) GIXRD patterns and (B) Raman spectra of TiO_2 thin film thermally treated in air at 110, 400 and 800 °C.*

Scanning Electron Microscopy (SEM) and Atomic Force Microscopy (AFM) measurements were performed, to gain further insights into the morphology and topography of the TiO_2 layers (see Figure 4). Indeed, previous studies have shown that the surface morphology of materials, and more specifically the roughness and cracks within the layers, can have a significant influence on the properties of TiN films [56,58–60].

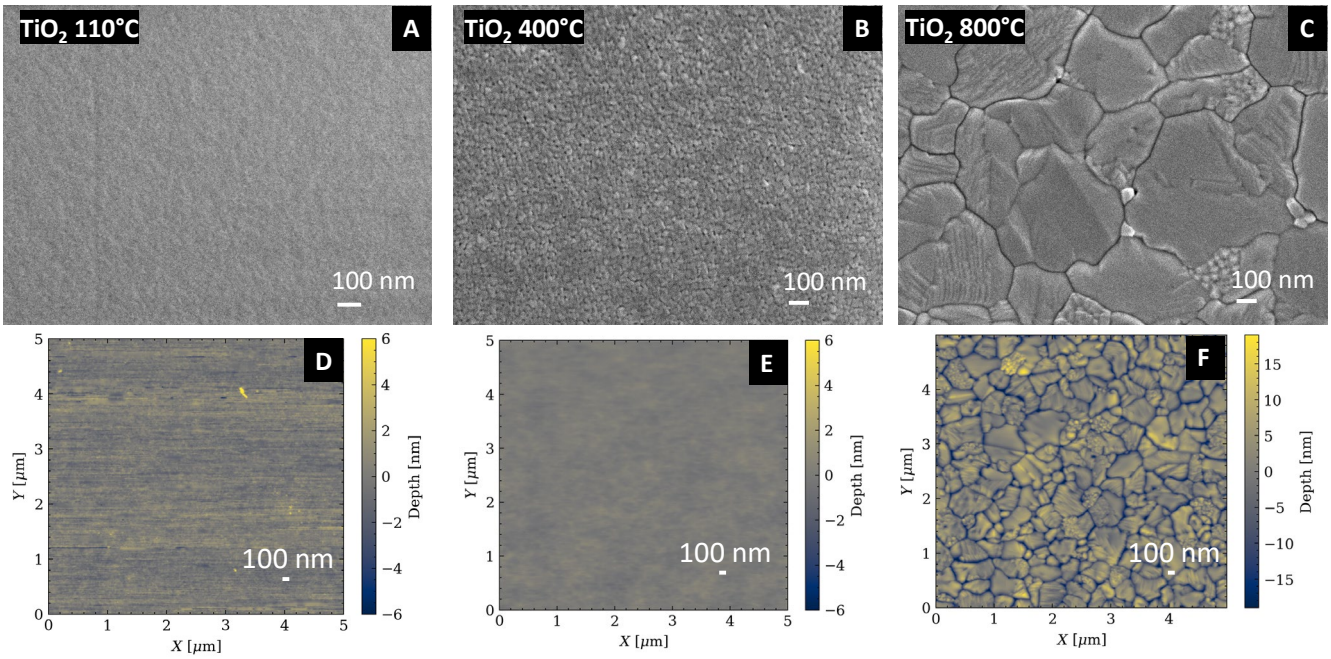

Figure 4: *(A), (B) and (C)SEM micrographs of TiO_2 thin film heat-treated in air respectively at 110°C, 400°C and 800°C and (D), (E) and (F) their corresponding AFM images.*

As can be seen in Figure 4, the SEM micrograph of the TiO_2 xerogel layer annealed at 110°C shows that the surface is very homogeneous with no real apparent porosity. The smoothness of the surface and the absence of cracks was confirmed by the AFM measurement by calculating the Root Mean Square surface roughness (R_{RMS}) in Figure 4D (R_{RMS} = 0.73 nm). After heat treatment at 400°C the surface of TiO_2 films resembles that of the previous sample with a homogeneous surface observable both in the SEM image and with the AFM measurement (Figure 4E). However, unlike the amorphous sample, slight cracks are apparent and the roughness is higher (R_{RMS} = 5.46 nm). A completely different morphology appeared after treatment at 800°C with very pronounced cracks, as can be seen in the SEM image and AFM measurement in Figure 4F (R_{RMS} = 6.84 nm). The results thus indicate that, as expected, increasing the annealing temperature increases the surface roughness of our TiO_2 films (Table 1), thereby confirming SEM observations.

	R_{RMS} (nm)
TiO_2 amorphous (110°C)	0.73
TiO_2 anatase (400°C)	5.46
TiO_2 rutile (800°C)	6.84

Table 1: *Roughness parameters of TiO_2 thin films annealed in air at different temperatures.*

These structural characterizations reveal disparities in the crystal structure of the initial TiO_2 films, as well as differences in their morphology and topography. The thermal treatments applied to each sample to obtain the different crystalline phases were not optimized, which could explain the appearance of cracks and defects under the high temperature treatment. These samples were then nitrided using the RTN process to obtain TiN thin films, and then characterized to highlight the influence of the initial crystalline phase of the TiO_2 on the different properties of the resulting TiN films.

3.2 Titanium nitride films

3.2.1 Optical properties

After treatment under NH_3, the resulting TiN films are visually identical, with a slightly transparent grayish color (Figure 5A) in transmission and gold color in reflection (Figure 5B). The thickness of the three TiN films measured by profilometry was around 50 nm ± 10 nm. The spectra in Figure 5 indicate very similar optical properties in transmission and reflection highlighting the metallic character of the layers. The transmittance spectra of the TiN thin films display a broad absorption peak at wavelength of around 480 nm with a maximum transmittance of 29% for TiN annealed at 110 °C versus 26% for TiN annealed at 400 °C and 800 °C, and then reduced to 1–2% in the near-infrared region. The broad absorption signal in the visible region due to the incorporation of nitrogen into the film is in agreement with the gray coloring of the TiN coatings. The reflectance spectra indicate a minimum reflectance of 17% at wavelengths around 480 nm for both TiN layers obtained from amorphous or anatase TiO_2 films, and minimum reflectance of around 12% for the TiN obtained from the rutile TiO_2 film. In the NIR region, the TiN layer obtained from amorphous TiO_2 is slightly more reflective than the other TiN layers, with a maximum reflection around 78% (versus 75% for TiN annealed at 400 °C and 800 °C).

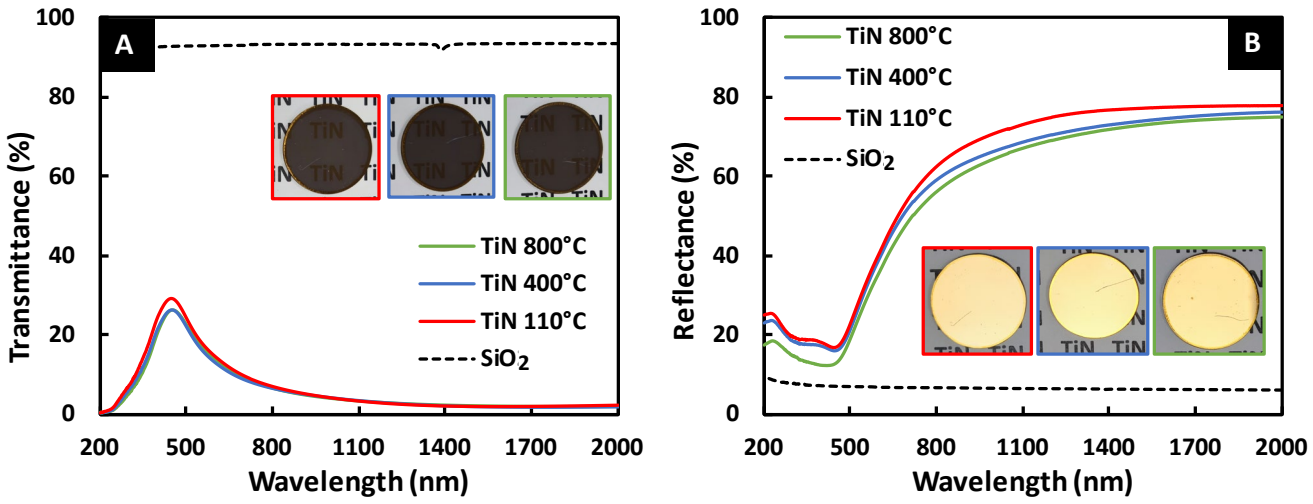

Figure 5: *(A) UV–Visible-NIR transmittance and (B) reflectance spectra of the SiO_2 substrate and TiN films from the nitriding of TiO_2 layers annealed in air at 110°C, 400°C and 800 °C. Inset: optical photographs of the different TiN thin films in specular transmission and reflection.*

3.2.2 Structure and surface morphology

GIXRD measurements and Raman spectra of the three samples nitridated are presented in Figure 6. The GIXRD diffractogram related to the three coatings layers (i.e. TiO_2 amorphous, anatase and rutile) after nitridation are similar with five diffraction peaks centered at 2θ = 36.75, 42.69, 61.96, 74.22 and 78.13° (Figure 6A). The Bragg indexation of the five peaks corresponds to a cubic phase with a space group $Fm\bar{3}m$ (JCPDS file 96-720-6076). The phase is in agreement with this space group and cell parameter value is osbornite TiN, whose

diffraction peaks within the investigated diffraction range correspond to the crystalline planes (111), (200), (220), (311), and (222). The Raman spectra of these TiN layers, presented in Figure 6B, clearly corroborate the previous GIXRD analysis. Indeed, regardless of the specific crystalline phase in which the initial TiO_2 film is subjected to nitridation, the resulting TiN thin film presents almost identical Raman vibration modes attributed to TiN, in accordance with results reported in previous works [6,7,35]. The 211, 320, 447 and 530 cm^{-1} bands observed in the spectrum relate to respectively, transverse acoustic (TA), longitudinal acoustic (LA), second-order acoustic (2A) and transverse optical (TO) modes of TiN.

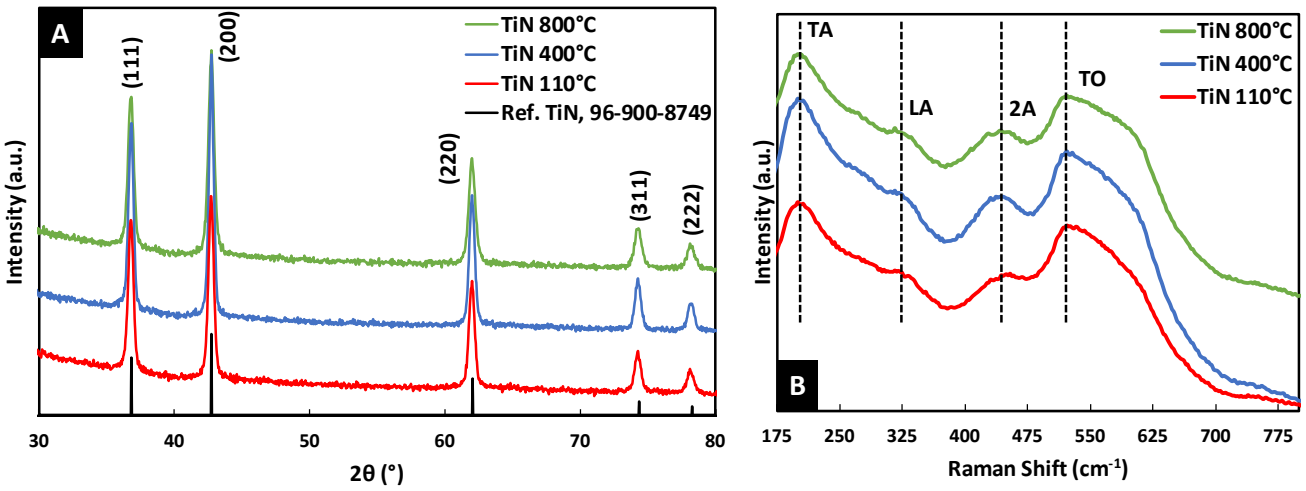

Figure 6: *(A) GIXRD patterns, (B) Raman spectra of the TiN films from the nitriding of TiO_2 layers annealed in air at 110, 400 and 800 °C.*

SEM micrographs of the resulting TiN layers after nitridation show different morphology depending on the initial state of the TiO_2 layer (Figure 7A, B and C). These images also clearly show a difference in morphology of the cracks, the size of the cracks appears to increase with increasing annealing temperature. At 110°C only small homogeneously distributed cracks are exhibited, at 400°C the size of the cracks is bigger, and at 800°C the surface is composed of the biggest cracks.

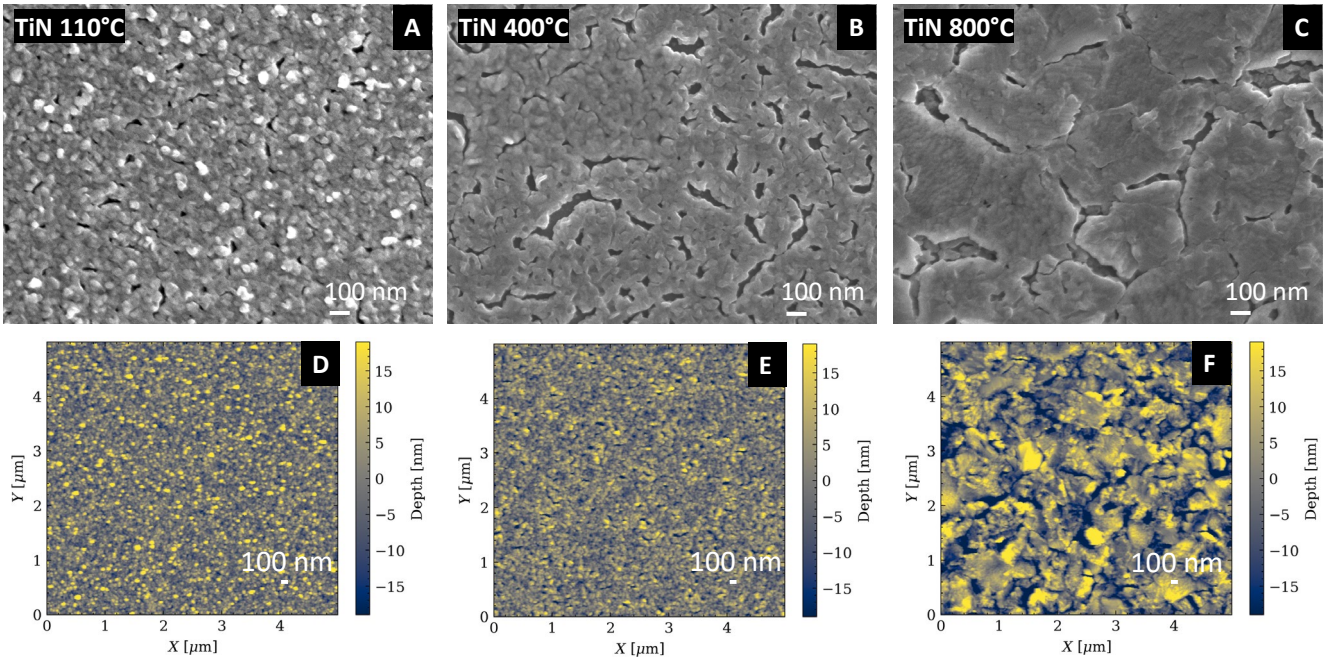

Figure 7: *(A), (B) and (C): SEM micrographs of TiN films resulting from the nitriding of TiO_2 layers annealed in air at 110, 400 and 800 °C respectively and (D), (E) and (F) their corresponding AFM images.*

The surface topography and surface roughness of TiN coatings are shown in Figure 7D, E and F. The roughness parameters R_{RMS}, deduced from mapping (listed in Table 2), are respectively 6.84 nm, 5.96 nm and 11.86 nm for TiN with increasing annealing temperatures.

	R_{RMS} (nm)
TiN (110°C)	6.84
TiN (400°C)	5.96
TiN (800°C)	11.86

Table 2: *Roughness parameters of TiN thin films after nitridation of amorphous, anatase and rutile TiO2 layers*

After nitridation the visual appearance and the structural characterization (GIXRD and Raman) show the complete nitridation of the three sample with no significant difference. Comparison of the surface morphology of the samples before and after the nitridation showed that the state of the surface was similar. Indeed, the main difference are the increase of the roughness and the cracks however the general appearance of the surface is similar. The increase of cracks can be explained by the film densification and the rapid crystalline phase change of TiO_2 during heat treatment. This effect of film shrinkage after nitridation by RTN had already been observed in previous studies [7,35]. In summary, whatever the initial state of the TiO_2 the RTN process allows the complete nitridation of the films. The substitution of the oxygen by the nitrogen occurs regardless the initial state of the TiO_2. Furthermore, by comparing the SEM and AFM measurements before and after nitridation it can be seen that the nitridation process does not modify significantly the surface morphology. Indeed, the only impact the nitridation seems to have on the surface is a slight increase in the size of the cracks, probably due to shrinkage of the films during the RTN process.

3.3 Properties of the titanium nitride films.

3.3.1 Plasmonic properties.

After analyzing the structure and the surface morphology of the TiN samples their plasmonic properties were compared to conclude on the impact of the initial state. Figure 8 shows the refractive index n (A) and the extinction coefficient k (B) of each sample measured by ellipsometry measurements. The real (ε') and the imaginary (ε'') part of the permittivity were deduced with the following equations and are respectively displayed in Figure 8C and 8D:

$$\varepsilon' = n^2 - k^2 \quad (1)$$

$$\varepsilon'' = 2nk \quad (2)$$

To evaluate the performances of the TiN thin films for plasmonic applications the figure of merit (FoM) [61] was determined from the deduced permittivity with the following equation:

$$FoM = \frac{\varepsilon'^2}{\varepsilon''} \quad (3)$$

The figure of merit is calculated with equation (3) in the case of surface plasmon polariton (SPP) [61]. It expresses the response of metallic layers to propagate surface plasmons, which is better when the FoM is high (low loss).

As can be seen in Figure 8, the allures of all the curves of each sample are similar. However, a slight difference in the extinction coefficient (k) is apparent in Figure 8B for high wavelength, this difference also affects their permittivities. Indeed at 1000 nm, the values of k, ε' and ε'' are respectively 4.17, -15.31 and -12.05 for the sample annealed at 110°C, 3.94, -13.50 and 11.27 for the sample annealed at 400 °C and 3.79, -12.59 and 10.00 for the sample annealed at 800 °C. This difference was expected, it originates from the difference of roughness and porosity of each film as it has been seen in Figure 7. As the size of the cracks and the roughness increase with the temperature of the annealing the losses increase leading to a diminution of the extinction coefficient k. The figure of merit in Figure 8E shows three nearly identical curves with an absorption peak at around 520 nm and a plateau of around 15 for high wavelengths, which is in agreement with the literature [24]. These values could appear low compared to those obtained in the case of noble metals gold or silver for which in the infrared range at a wavelength of λ=1000 nm the FoM values are respectively around 1000 and 10000 [62]. However, unlike gold and silver, TiN has a much higher thermal resistance, making it ideal for plasmonic applications at high temperatures.

It should be noted that these results for TiN are quite similar to those obtained in previous work [6,35] and in the literature shown in Figure 8E [24]. A slight shift of 20 nm of the dip can be observed due to the slight difference observed in the real part of the permittivity near 0.

Thus, as stated in these studies a metallic behavior of the TiN is observed no matter the initial state of the TiO_2 for wavelengths greater than 530nm.

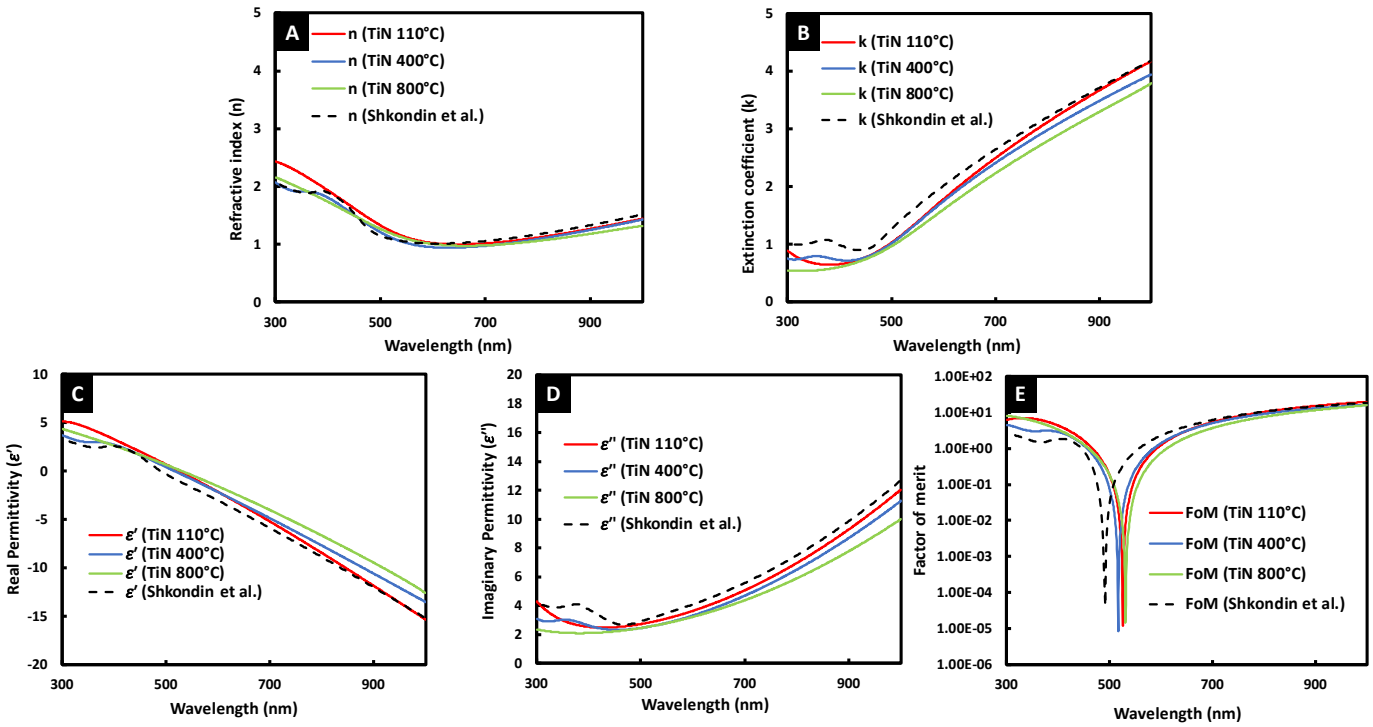

Figure 8: *(A) Refractive index (n) and (B) extinction coefficient (k) spectra of the three TiN layers. (C) Real part and (D) imaginary part of the permittivity for the TiN films. (E) Factor of merit for the different TiN layers.*

3.3.2 Friction behavior

Figure 9 shows changes in the friction coefficient as a function of the number of sliding cycles of the TiN coatings tested against the stainless-steel ball in reciprocating sliding contact. For TiN layers from amorphous and anatase TiO_2, the friction coefficient remained relatively stable at an average value of 0.15 and 0.10 during the 100 sliding cycles. This friction coefficient range is close to the values reported for typical dense TiN films deposited using a PVD process [63]. However, a TiN layer resulting from rutile TiO_2 presented a higher friction coefficient than the other two TiN coatings, i.e., the coefficient increased from 0.2 to almost 0.4 after 100 sliding cycles. This could be explained by the non-uniform morphology of this TiN coating, as can be seen in the SEM/AFM images in Figure 7C and 7F, which can influence the friction during the test [64]. The friction test showed that TiN film exhibits low dry friction with negligible wear at the scale of 100 sliding cycles. Longer tribological tests are necessary to quantify the wear resistance of the TiN films with a view to using the film for a variety of industrial applications.

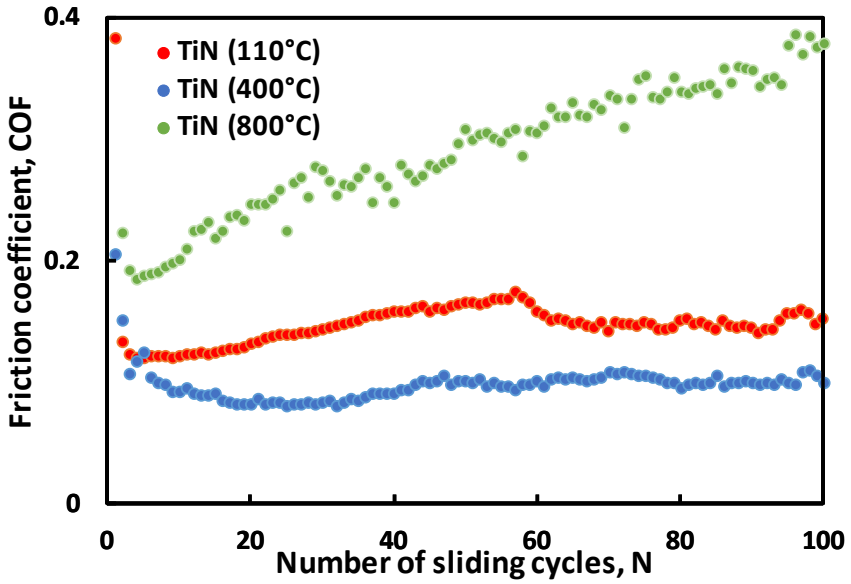

Figure 9: *Friction coefficient evolution, versus the number of sliding frictions, of the different TiN films in reciprocating sliding contact against a stainless-steel ball*

4. CONCLUSIONS

This paper provides proof that nitridation of the crystalline phases (amorphous, anatase and rutile) of the TiO_2 is possible. Raman spectroscopy and X-ray diffraction showed complete nitridation of each sample regardless of the crystalline phase. The effect of the initial crystalline state of TiO_2 on the plasmonic and mechanical properties of TiN thin films obtained using a rapid thermal nitridation process were also investigated. After the elaboration and the analysis of the crystal structure and surface morphology of the amorphous, anatase and rutile TiO_2 thin films, the samples were nitridated. DRX and Raman spectroscopy of the resulting TiN thin films confirmed the complete nitridation of each sample. The main difference between the layers was the state of their surface observed using SEM and AFM measurements. Indeed, each TiN has a different surface morphology but the surface morphology of the TiO_2 and its associated TiN are similar. Nitridation only seems to further densify the layers, widening the size of the cracks that are already present. Thus, the surface morphology of the TiN thin films seems to only depend on the surface morphology before nitridation. The optical properties of the TiN layers obtained were compared. A slight difference was found in the plasmonic properties that can be explained by the difference in the surface morphology (cracks and roughness) of each layer. The friction coefficient of the TiN layers from amorphous and anatase TiO_2 is similar and close to values reported in the literature. However, the TiN layer resulting from rutile TiO_2 presents a higher friction coefficient probably due to the non-uniform morphology of this TiN coating.

The simplicity and versatility of this nitridation technique allows it to work with every crystal structure of TiO_2. Furthermore, the TiO_2 used in this article was produced using a sol-gel route, meaning the RTN can be applied to other forms of TiO_2 including powder, dense films or even fibers. The high compatibility and uniformity of this new nitridation technique makes it suitable to produce TiN for a wide range of fields, including chemistry [65], medicine [66], energy [67], mechanics [68] and plasmonics [27].

DECLARATION OF COMPETING INTEREST

The authors declare that they have no known competing financial interests or personal relationships that could have appeared to influence the work reported in this paper.

DATA AVAILABILITY

Data will be made available on requested.

ACKNOWLEDGEMENT

The authors acknowledge the French National Research Agency (ANR) for financial support in the framework of project NITRURATION (ANR-21-CE08-0042-01), and the Centre National de la Recherche Scientifique CNRS (French RENATECH+, nano-SaintEtienne plateform).

REFERENCES

1. Giordano, C. & Antonietti, M. Synthesis of crystalline metal nitride and metal carbide nanostructures by sol–gel chemistry. *Nano Today* **6**, 366–380 (2011).

2. Rasaki, S. A., Zhang, B., Anbalgam, K., Thomas, T. & Yang, M. Synthesis and application of nano-structured metal nitrides and carbides: A review. *Progress in Solid State Chemistry* **50**, 1–15 (2018).

3. Sproul, W. D. Reactively sputtered nitrides and carbides of titanium, zirconium, and hafnium. *Journal of Vacuum Science & Technology A: Vacuum, Surfaces, and Films* **4**, 2874–2878 (1986).

4. Ming'e, W., Guojia, M., Xing, L. & Chuang, D. Morphology and Mechanical Properties of TiN Coatings Prepared with Different PVD Methods. *Rare Metal Materials and Engineering* **45**, 3080–3084 (2016).

5. Gagnon, G. *et al.* Characterization of reactively evaporated TiN layers for diffusion barrier applications. *Journal of Applied Physics* **75**, 1565–1570 (1994).

6. Valour, A. *et al.* Optical, electrical and mechanical properties of TiN thin film obtained from a TiO2 sol-gel coating and rapid thermal nitridation. *Surface and Coatings Technology* **413**, 127089 (2021).

7. Crespo-Monteiro, N. *et al.* Micro-nanostructured plasmonic TiN layer produced using rapid thermal nitridation of a nanoimprinted TiO_2 sol-gel. *Opt. Mater. Express* **12**, 3846 (2022).

8. Roberts, A. S. *et al.* Ultra-thin titanium nitride films for refractory spectral selectivity [Invited]. *Opt. Mater. Express* **8**, 3717 (2018).

9. Chang, C.-C. *et al.* Highly Plasmonic Titanium Nitride by Room-Temperature Sputtering. *Sci Rep* **9**, 15287 (2019).

10. Guo, B. *et al.* Microstructure and tribological properties of in situ synthesized TiN/Ti3Al intermetallic matrix composite coatings on titanium by laser cladding and laser nitriding. *Materials Science and Engineering: A* **480**, 404–410 (2008).

11. Li, W. *et al.* Refractory Plasmonics with Titanium Nitride: Broadband Metamaterial Absorber. *Adv. Mater.* **26**, 7959–7965 (2014).

12. Choudhury, S. M. *et al.* Material platforms for optical metasurfaces. *Nanophotonics* **7**, 959–987 (2018).

13. Kildishev, A. V., Boltasseva, A. & Shalaev, V. M. Planar Photonics with Metasurfaces. *Science* **339**, 1232009 (2013).

14. Kim, T.-S., Park, S.-S. & Lee, B.-T. Characterization of nano-structured TiN thin films prepared by R.F. magnetron sputtering. *Materials Letters* **59**, 3929–3932 (2005).

15. Jafari, A. *et al.* Effects of Annealing on TiN Thin Film Growth by DC Magnetron Sputtering. *Advances in Mechanical Engineering* **6**, 373847 (2014).

16. Naik, G. V. *et al.* Epitaxial superlattices with titanium nitride as a plasmonic component for optical hyperbolic metamaterials. *Proc. Natl. Acad. Sci. U.S.A.* **111**, 7546–7551 (2014).

17. Prayakarao, S. *et al.* Gyroidal titanium nitride as nonmetallic metamaterial. *Opt. Mater. Express* **5**, 1316 (2015).

18. Krockenberger, Y., Karimoto, S., Yamamoto, H. & Semba, K. Coherent growth of superconducting TiN thin films by plasma enhanced molecular beam epitaxy. *Journal of Applied Physics* **112**, 083920 (2012).

19. Guo, W.-P. *et al.* Titanium Nitride Epitaxial Films as a Plasmonic Material Platform: Alternative to Gold. *ACS Photonics* **6**, 1848–1854 (2019).

20. Rebenne, H. E. & Bhat, D. G. Review of CVD TiN coatings for wear-resistant applications: deposition processes, properties and performance. *Surface and Coatings Technology* **63**, 1–13 (1994).

21. Fix, R., Gordon, R. G. & Hoffman, D. M. Chemical vapor deposition of titanium, zirconium, and hafnium nitride thin films. *Chem. Mater.* **3**, 1138–1148 (1991).

22. Langereis, E., Heil, S. B. S., Van De Sanden, M. C. M. & Kessels, W. M. M. *In situ* spectroscopic ellipsometry study on the growth of ultrathin TiN films by plasma-assisted atomic layer deposition. *Journal of Applied Physics* **100**, 023534 (2006).

23. Briggs, J. A. *et al.* Fully CMOS-compatible titanium nitride nanoantennas. *Applied Physics Letters* **108**, 051110 (2016).

24. Shkondin, E., Repän, T., Takayama, O. & Lavrinenko, A. V. High aspect ratio titanium nitride trench structures as plasmonic biosensor. *Opt. Mater. Express* **7**, 4171 (2017).

25. Yu, I.-S. *et al.* Substrate-insensitive atomic layer deposition of plasmonic titanium nitride films. *Opt. Mater. Express* **7**, 777 (2017).

26. Murai, S. *et al.* Plasmonic arrays of titanium nitride nanoparticles fabricated from epitaxial thin films. *Opt. Express* **24**, 1143 (2016).

27. Sugavaneshwar, R. P. *et al.* Fabrication of Highly Metallic TiN Films by Pulsed Laser Deposition Method for Plasmonic Applications. *ACS Photonics* **5**, 814–819 (2018).

28. Wang, Z., Zhang, B., Gao, K. & Liu, R. Adjustable TiN coatings deposited with HiPIMS on titanium bipolar plates for PEMFC. *International Journal of Hydrogen Energy* **47**, 39215–39224 (2022).

29. Yu, J. *et al.* Titanium Nitride Electron-Conductive Contact for Silicon Solar Cells By Radio Frequency Sputtering from a TiN Target. *ACS Appl. Mater. Interfaces* **12**, 26177–26183 (2020).

30. Su, J., Boichot, R., Blanquet, E., Mercier, F. & Pons, M. Chemical vapor deposition of titanium nitride thin films: kinetics and experiments. *CrystEngComm* **21**, 3974–3981 (2019).

31. Kamiya, K., Nishijima, T. & Tanaka, K. Nitridation of the Sol-Gel-Derived Titanium Oxide Films by Heating in Ammonia Gas. *J American Ceramic Society* **73**, 2750–2752 (1990).

32. Mangamma, G. *et al.* Synthesis and gas phase nitridation of nanocrystalline TiO_2. *J. Phys. D: Appl. Phys.* **40**, 4597–4602 (2007).

33. Zhang, H., Li, F. & Jia, Q. Preparation of titanium nitride ultrafine powders by sol–gel and microwave carbothermal reduction nitridation methods. *Ceramics International* **35**, 1071–1075 (2009).

34. Shi, H. *et al.* Synthesis of TiN nanostructures by Mg-assisted nitriding TiO2 in N2 for lithium ion storage. *Chemical Engineering Journal* **336**, 12–19 (2018).

35. Valour, A. *et al.* Micro–Nanostructured TiN Thin Film: Synthesis from a Photo-Patternable TiO_2 Sol–Gel Coating and Rapid Thermal Nitridation. *J. Phys. Chem. C* **124**, 25480–25488 (2020).

36. Crespo-Monteiro, N. *et al.* Versatile Zirconium Oxide (ZrO2) Sol-Gel Development for the Micro-Structuring of Various Substrates (Nature and Shape) by Optical and Nano-Imprint Lithography. *Materials* **15**, 5596 (2022).

37. Wen-Cheun Au, B., Chan, K.-Y. & Knipp, D. Effect of film thickness on electrochromic performance of sol-gel deposited tungsten oxide (WO3). *Optical Materials* **94**, 387–392 (2019).

38. Pookmanee, P. & Phanichphant, S. Titanium dioxide powder prepared by a sol-gel method.

39. You, Y., Zhang, S., Wan, L. & Xu, D. Preparation of continuous TiO2 fibers by sol–gel method and its photocatalytic degradation on formaldehyde. *Applied Surface Science* **258**, 3469–3474 (2012).

40. Priyalakshmi Devi, K., Goswami, P. & Chaturvedi, H. Fabrication of nanocrystalline TiO2 thin films using Sol-Gel spin coating technology and investigation of its structural, morphology and optical characteristics. *Applied Surface Science* **591**, 153226 (2022).

41. Mechiakh, R., Sedrine, N. B., Chtourou, R. & Bensaha, R. Correlation between microstructure and optical properties of nano-crystalline TiO2 thin films prepared by sol–gel dip coating. *Applied Surface Science* **257**, 670–676 (2010).

42. Arconada, N. *et al.* Synthesis and photocatalytic properties of dense and porous TiO2-anatase thin films prepared by sol–gel. *Applied Catalysis B: Environmental* **86**, 1–7 (2009).

43. Campostrini, R., Carturan, G., Palmisano, L., Schiavello, M. & Sclafani, A. Sol-gel derived anatase Ti02: morphology and photoactivity.

44. Aghababazadeh, R. *et al.* Synthesis and characterization of nanocrystalline titanium nitride powder from rutile and anatase as precursors. *Surface Science* **601**, 2881–2885 (2007).

45. Saidi, A., Setoudeh, N. & Welham, N. J. Production of Titanium Nitride by Carbothermic Reduction of the Anatase and Rutile Forms of Titanium Dioxide. *MSF* **539–543**, 2743–2748 (2007).

46. White, G. V., Mackenzie, K. J. D., Brown, I. W. M. & Johnston, J. H. Carbothermal synthesis of titanium nitride: Part III Kinetics and mechanism. *J Mater Sci* **27**, 4300–4304 (1992).

47. Sato, R., Ishii, S., Nagao, T., Naito, M. & Takeda, Y. Broadband Plasmon Resonance Enhanced Third-Order Optical Nonlinearity in Refractory Titanium Nitride Nanostructures. *ACS Photonics* **5**, 3452–3458 (2018).

48. Sobell, Z. C. & George, S. M. Electron-Enhanced Atomic Layer Deposition of Titanium Nitride Films Using an Ammonia Reactive Background Gas. *Chem. Mater.* **34**, 9624–9633 (2022).

49. White, N. *et al.* Surface/interface analysis and optical properties of RF sputter-deposited nanocrystalline titanium nitride thin films. *Applied Surface Science* **292**, 74–85 (2014).

50. Tian, J. *et al.* A novel triple-porosity model for fractured-vuggy reservoirs based on Maxwell-Garnett mixing rule. *Journal of Petroleum Science and Engineering* **208**, 109362 (2022).

51. Petrik, P. *et al.* Comparative study of surface roughness measured on polysilicon using spectroscopic ellipsometry and atomic force microscopy. *Thin Solid Films* **315**, 186–191 (1998).

52. Kubelka, P. & Munk, F. An Article on Optics of Paint Layers. *Z. Techn. Physik.* **12**, 593–601 (1931).

53. Oda, S., Uchiyama, H. & Kozuka, H. Thermoplasticity of sol–gel-derived titanoxanes chemically modified with benzoylacetone. *J Sol-Gel Sci Technol* **70**, 441–450 (2014).

54. El-Deen, S. S. *et al.* Anatase TiO2 nanoparticles for lithium-ion batteries. *Ionics* **24**, 2925–2934 (2018).

55. Frank, O. *et al.* Raman spectra of titanium dioxide (anatase, rutile) with identified oxygen isotopes (16, 17, 18). *Phys. Chem. Chem. Phys.* **14**, 14567 (2012).

56. Mazza, T. *et al.* Raman spectroscopy characterization of Ti O 2 rutile nanocrystals. *Phys. Rev. B* **75**, 045416 (2007).

57. Praveen, P. & Sagayaraj, R. Structural, Functional and Optical Characters of TiO2 Nanocrystallites: Anatase and Rutile Phase. *St. Joseph's Journal of Humanities and Science* **6**, 43–53 (2019).

58. Achour, A. *et al.* Titanium nitride films for micro-supercapacitors: Effect of surface chemistry and film morphology on the capacitance. *Journal of Power Sources* **300**, 525–532 (2015).

59. Islam, Md. S. & Zubair, A. Plasmon tuning in ultra-thin titanium nitride films. *Opt. Continuum* **2**, 1688 (2023).

60. Sun, N. *et al.* Sputtered titanium nitride films with finely tailored surface activity and porosity for high performance on-chip micro-supercapacitors. *Journal of Power Sources* **489**, 229406 (2021).

61. West, P. R. *et al.* Searching for better plasmonic materials. *Laser & Photon. Rev.* **4**, 795–808 (2010).

62. Maurya, K. C., Shalaev, V. M., Boltasseva, A. & Saha, B. Reduced optical losses in refractory plasmonic titanium nitride thin films deposited with molecular beam epitaxy. *Opt. Mater. Express* **10**, 2679 (2020).

63. Wróblewski, P. & Rogólski, R. Experimental Analysis of the Influence of the Application of TiN, TiAlN, CrN and DLC1 Coatings on the Friction Losses in an Aviation Internal Combustion Engine Intended for the Propulsion of Ultralight Aircraft. *Materials* **14**, 6839 (2021).

64. Silva, W. M., Souza, P. S. & Carneiro, J. R. Methods of data analysis for the ball cratering test on TiN and DLC coated steel. *Mat. Res.* **19**, 9–17 (2016).

65. Sarkar, K. *et al.* Enhancement in corrosion resistance and vibration damping performance in titanium by titanium nitride coating. *SN Appl. Sci.* **2**, 949 (2020).

66. Duta, L. *et al.* Thickness Influence on In Vitro Biocompatibility of Titanium Nitride Thin Films Synthesized by Pulsed Laser Deposition. *Materials* **9**, 38 (2016).

67. Zhang, J., Hu, H., Liu, X. & Li, D.-S. Development of the applications of titanium nitride in fuel cells. *Materials Today Chemistry* **11**, 42–59 (2019).

68. Galetz, M. C., Seiferth, S. H., Theile, B. & Glatzel, U. Potential for adhesive wear in friction couples of UHMWPE running against oxidized zirconium, titanium nitride coatings, and cobalt-chromium alloys. *J. Biomed. Mater. Res.* **93B**, 468–475 (2010).